states $\psi_a\varphi_a$ and $\psi_b\varphi_b$, where ψ_a and ψ_b are Γ_8 states of $^4T_2$ or $^4T_1$ chosen to be diagonal in $\mathcal{H}_{1s}$. Since ψ_a and ψ_b have different energies, for exact degeneracy, $\varphi_a \neq \varphi_b$. We ignore this complication, which should not be important when $G_2(\omega)$ is slowly varying, and combine ψ_a and ψ_b to form ψ_1 before forming the Born-Oppenheimer product $\psi_1\varphi_1$.

[27]Note that $P_\beta \sim N_0^{-1/2}$, where N_0 is the total number of ions in the crystal [see Ref. 24, Eq. (6.1)].

[28]Yu. E. Perlin, Usp. Fiz. Nauk. 80, 553 (1963) [Soviet Phys. Usp. 6, 542 (1964)].

[29]D. F. Nelson and M. D. Sturge, Phys. Rev. 137, A1117 (1965).

[30]D. S. McClure, J. Chem. Phys. 36, 2757 (1962).

[31]Y. Tanabe and S. Sugano, J. Phys. Soc. Japan 9, 766 (1954).

[32]S. Sugano and Y. Tanabe, J. Phys. Soc. Japan 13, 880 (1958).

[33]J. S. Griffith, *Irreducible Tensor Method for Molecular Symmetry Groups* (Prentice-Hall, Englewood Cliffs, N. J., 1962). We have checked the relevant parts of his Table E1.

PHYSICAL REVIEW B VOLUME 2, NUMBER 7 1 OCTOBER 1970

Self-Induced Transparency in Acoustic Paramagnetic Resonance

N. S. Shiren*
IBM, Thomas J. Watson Research Center, Yorktown Heights, New York 10598
(Received 24 February 1970)

Experiments on the propagation of microwave ultrasonic pulses through a resonant absorber are described. The principal features of self-induced transparency as described by McCall and Hahn for light pulses are observed. Quantitative measurements of pulse delay, output pulse width, energy, and area are in fair agreement with a calculation by Hopf which accounts approximately for the effect of the single reflection present in most of the experiments. Multiply reflected pulses exhibited linearly cumulative delay times, indicating constant reduced velocity during successive traversals through the absorber. Coherence-induced pulse breakup is shown to be a possible explanation of the pulse distortion and modulation observed in acoustic-paramagnetic-resonance experiments on Fe^{2+}.

I. INTRODUCTION

Several years ago the author reported that[1] the attenuation of microwave ultrasonic pulses by electron-spin-resonance transitions was accompanied by a large decrease in pulse velocity below the normal value in the host crystal. Velocity measurements were compared with small signal linear theories of signal velocity in a region of resonance absorption, as derived by Brillouin and by Baerwald.[2] Fair agreement was found if certain assumptions were made regarding the spatial distribution of the mechanism responsible for inhomogeneous broadening, and if it was also assumed that the transverse damping time of the spin system was shorter than the pulse width. While these observations utilized Ni^{2+} and Fe^{2+} impurities in MgO, the effect has also been observed by others on U^{4+} in CaF_2.[3]

More recently, McCall and Hahn[4] (MH) have derived a theory of electromagnetic pulse propagation including source terms, in Maxwell's equations, due to the coherently driven polarization of a two-level quantum-mechanical system. Under the condition that the pulse width is short compared with all damping time constants, pulses were found to propagate with greatly reduced velocities.

If one defines a pulse area

$$\theta(z) = (2p/\hbar) \int_{-\infty}^{\infty} \mathcal{E}(z,t)dt \ ,$$

where p is the average electric dipole moment and $\mathcal{E}(z,t)$ is the electric field amplitude of a circularly polarized plane-wave pulse propagating along z, then θ is also the turning angle of dipoles at resonance. For input areas greater than a threshold value, $\theta = \pi$, MH find that after an initial reshaping and energy loss, steady-state pulses develop and no further energy loss occurs. They term this "self-induced transparency" (SIT).

Analytic solutions show that the steady-state pulses have areas $\theta = 2\pi n$ (n an integer), and for $n = 1$, the amplitude is

$$\mathcal{E}(z,t) = \frac{\hbar}{p\tau} \operatorname{sech}\left(\frac{t - z/V}{\tau}\right) \ .$$

The pulse delay is given by

$$1/V - 1/c = \tfrac{1}{2}\alpha\tau \ \text{sec/cm},$$

where c is the velocity in the nonresonant host, and the Beer's law energy absorption for very small-amplitude pulses is $e^{-\alpha z}$. Computer solutions carried out by Hopf and Scully[5] confirm the theory of MH and also show that the pulse delays are even larger than above for input areas $\pi \leq \theta < 2\pi$.

Since measurements (reported in this paper) show that the shortest damping time T_2 of Ni^{2+} and Fe^{2+} in MgO can be larger than the input ultrasonic pulse widths, the author has redone the experiments in the light of the theory of MH. While the earlier work was done on systems with $\alpha L \approx 1$, in all the measurements reported in this paper $\alpha L \gtrsim 8$. (L is the total propagation path length in the host crystal.) Also, wider bandwidth equipment was used in order to avoid the output pulse distortion which was present earlier.

There are several advantages to using microwave ultrasonic pulses and spin resonance, rather than optical methods, in SIT experiments: Input pulse shapes are repeatable at high repetition rates; the quantum-mechanical nature of the resonant transitions is generally simpler; the input and/or transition frequencies are continuously variable; the input pulse width is variable. On the other hand, there are also comparative disadvantages, such as the impossibility of obtaining good impedance matching at the output, so that standing wave regions are always present. Also, detectors are less sensitive, and the best methods measure integrated amplitude (across the detector plane) rather than energy, and so are sensitive to misalignment of transducers and propagation medium, and to refraction.

In the work reported here, the reflected echo technique was used. The measurements are thus not directly comparable with the MH theory since the latter was derived for a single traversal through the medium rather than a round trip. However, Hopf has performed a computer calculation for the double traversal, utilizing parameters applicable to some of my experimental runs.[6] Agreement of the experimental results with this theory, while not exact, definitely shows that the pulse delays are due to SIT and not to the linear theory of signal velocity. In addition, all the distinctive features of SIT were observed. The output pulse shapes were nearly hyperbolic secant; in some experiments a transparency condition was approached; pulse break up was observed for larger input areas.

In Sec. II the theory of SIT is shown to be applicable to ultrasonic pulses interacting with spin $S=1$ systems; certain modifications introduced by Rhodes *et al.*[7] are shown to be not applicable to the present work; Hopf's results are presented; the effect of nonresonant host absorption is considered; and SIT is compared with saturation or "hole burning."

The experimental techniques are discussed in Sec. III. The results are contained in Sec. IV, and in Sec. V they are compared with theory and with the author's earlier work as well as that of others. It is also shown that coherence effects can explain certain other phenomena observed in pulsed acoustic paramagnetic resonance (APR).

In the Appendix the formalism of Sec. II is used to derive a dispersion relation for APR which agrees with that previously found by Jacobsen and Stevens.[8]

II. THEORY

A. Coherence Effects in Pulsed APR

Although it appears intuitively obvious that the MH theory of SIT for light waves should apply equally well to any plane-wave propagation in the presence of resonance absorption, it is worthwhile to demonstrate that an equivalent formalism exists in the case of pulsed APR. Specifically, we consider the problem at hand, namely, spin $S=1$ systems in (O_h) symmetry at microwave frequencies. Other spin systems may be treated similarly.

In the spin-Hamiltonian formalism,

$$\mathcal{H} = \mathcal{H}_0 + \mathcal{H}_c + \mathcal{H}_{SL}\,; \quad \mathcal{H}_0 = \hbar\gamma \vec{H}\cdot\vec{S} \tag{1}$$

is the Zeeman splitting by the applied dc magnetic field $\vec{H}$; γ is the gyromagnetic ratio. In (O_h) symmetry this term results in three equally spaced energy levels ($\langle S_z\rangle = -1, 0, +1$) and three possible ultrasonic transitions $\langle S_z\rangle = 0, \pm 1 (\Delta\langle S_z\rangle = \pm 1)$ with frequency $\gamma H/2\pi$, and $\langle S_z\rangle = \pm 1, \mp 1 (\Delta\langle S_z\rangle = \pm 2)$ with frequency $\gamma H/\pi$. However, small local departures from cubic symmetry caused by randomly distributed static strains shift the level separations, giving rise to inhomogeneous broadening of the resonance lines.[9] This is described by a crystal-field splitting term

$$\mathcal{H}_{SL} = \hbar\gamma \vec{H}\cdot\vec{\vec{E}}\cdot\vec{S} + \vec{S}\cdot\vec{\vec{D}}\cdot\vec{S}\,, \tag{2}$$

where the magnitudes of $\vec{\vec{E}}$ and $\vec{\vec{D}}$ are assumed randomly distributed over the various spin sites. We shall omit off-diagonal matrix elements of $\mathcal{H}_{SL}$ except insofar as they contribute to inhomogeneous broadening. That is, we neglect mixing of the pure Zeeman wave functions but keep diagonal matrix elements up to second order in perturbation theory. Later we will justify this for Fe^{2+} and Ni^{2+} in MgO;

$$\mathcal{H}_c = \vec{S}\cdot\vec{\vec{d}}\cdot\vec{S} \tag{3}$$

couples the spin system to the driving acoustic field through the tensor $\vec{\vec{d}}$ which is proportional to the applied strain and therefore both time and space dependent. A term of the form $\hbar\gamma \vec{H}\cdot\vec{\vec{\epsilon}}\cdot\vec{S}$ has been omitted from $\mathcal{H}_c$, and this will also be justified later.

The elements of $\vec{\vec{d}}$ are

$$d_{ij} = \sum_{kl} G_{ijkl}\, e_{kl} \quad (i,j,k = 1\cdots 3)\,, \tag{4}$$

where the G_{ijkl} are the spin-phonon coupling constants and e_{kl} are applied strains. In O_h symmetry, there are only two independent elements of $\vec{\vec{G}}$, G_{11} ($= -2G_{12}$) and G_{44} (in Voigt notation with 1, 2, 3 referring to cubic axes). Thus for a longitudinal

wave propagating on $\langle 100\rangle = z$,

$$\mathcal{H}_c = \tfrac{1}{2} G_{11} e_{zz} (2S_z^2 - S_x^2 - S_y^2)$$

$$= \tfrac{3}{2} G_{11} e_{zz} [S_z^2 - \tfrac{1}{3} S(S+1)]. \qquad (5)$$

Quantizing along the dc magnetic field axis z at angle Θ to z in the $y' = y$ plane, this becomes

$$\mathcal{H}_c = \tfrac{3}{2} G_{11} e_{zz} [S_{z'}^2 \cos^2\Theta + S_{x'}^2 \sin^2\Theta$$

$$+ (S_{x'} S_{z'} + S_{z'} S_{x'}) \sin 2\Theta] .$$

Following MH we write

$$e_{zz} = 2\mathcal{E}(z,t) \cos[\omega t - kz - \phi(z)] , \qquad (6)$$

where $\phi(z)$ and $\mathcal{E}(z,t)$ are assumed slowly varying in the sense that $|\partial\phi/\partial z| \ll k$, $|\partial\mathcal{E}/\partial z \ll k|\mathcal{E}|$, and $|\partial\mathcal{E}/\partial t| \ll \omega|\mathcal{E}|$, where $k = \omega/c$ is the off-resonance magnitude of the wave vector and ϕ is an arbitrary phase angle independent of the time t.

Because we are treating a longitudinal strain polarization, it is not possible to consider real circular polarizations. However, as is usual in resonance problems, we solve the coupled field and density matrix equations in the rotating wave approximation. Then, with the previously noted approximations on $\mathcal{H}_c$ and $\mathcal{H}_{SL}$, and labeling the states $a, b, c = -1, 0, +1$, respectively, we have

$$\|\mathcal{H}\| \approx \hbar \begin{bmatrix} \omega_a & \kappa_1 e_+ & \kappa_2 e_+ \\ \kappa_1 e_+^* & \omega_b & \kappa_1 e_+ \\ \kappa_2 e_+^* & \kappa_1 e_+^* & \omega_c \end{bmatrix} , \qquad (7)$$

where

$$e_+ = \mathcal{E}(z,t) e^{i[\omega t - kz - \phi(z)]},$$

$$\hbar\kappa_1 = \tfrac{3}{4} G_{11} \sin 2\Theta \left\langle \begin{matrix} a, b \\ b, c \end{matrix} \middle| S_\mp S_{z'} + S_{z'} S_\mp \middle| \begin{matrix} b, c \\ a, b \end{matrix} \right\rangle ,$$

$$\hbar\kappa_2 = \tfrac{3}{8} G_{11} \sin^2\Theta \left\langle \begin{matrix} a \\ c \end{matrix} \middle| S_\mp^2 \middle| \begin{matrix} c \\ a \end{matrix} \right\rangle , \qquad (8)$$

$$S_- = (S_{x'} - iS_{y'}), \qquad S_+ = (S_{x'} + iS_{y'}) .$$

$\omega_a + \omega_b + \omega_c = 0$, and $\hbar\omega_a, \hbar\omega_b, \hbar\omega_c$ are assumed to include the level displacements due to $\mathcal{H}_{SL}$. The diagonal unitary transformation, $U(t) = (e^{i\mu t}, 1, e^{-i\mu t})$, is identical to transforming to a coordinate system rotating about $\vec{H}$ (z' axis) with angular velocity μ if the original basis set are the pure Zeeman wave functions, as they are here. The effective Hamiltonian in this frame is

$$\|\mathcal{H}'\| = U^\dagger \, |\mathcal{H}| \, U + i\dot{U}^\dagger U$$

$$= \hbar \begin{bmatrix} (\omega_a + \mu) & \kappa_1 e_+ e^{-i\mu t} & \kappa_2 e_+ e^{-2i\mu t} \\ \kappa_1 e_+^* e^{i\mu t} & \omega_b & \kappa_1 e_+ e^{-i\mu t} \\ \kappa_2 e_+^* e^{2i\mu t} & \kappa_1 e_+^* e^{i\mu t} & (\omega_c - \mu) \end{bmatrix} . \qquad (9)$$

Note that resonance occurs for the $\Delta\langle S_z\rangle = \pm 2$ transition when $2\mu = \omega$ and $\omega = (\omega_c - \omega_a)$, while for $\Delta\langle S_z\rangle = \pm 1$ resonance requires $\mu = \omega$ with either (or both) $(\omega_a - \omega_b) = -\mu$, $(\omega_c - \omega_b) = +\mu$. In the absence of inhomogeneous broadening, $\omega_b = 0$, $\omega_a = -\omega_c$, and the resonance rotating frame is at the Larmor frequency regardless of the particular transition being studied.

The wave equation for the displacement u in the k direction is

$$\rho \frac{\partial^2 u}{\partial t^2} = \frac{\partial T_{zz}}{\partial z} + \frac{\partial T_{xz}}{\partial x} + \frac{\partial T_{yz}}{\partial y} .$$

T_{ij} are stress components equal to the derivatives of the internal energy density with respect to e_{ij}. Since $e_{zz} = \partial u/\partial z$, the resulting wave equation for e_{zz} is

$$\frac{\partial^2 e}{\partial z^2} - \frac{1}{c^2} \frac{\partial^2 e}{\partial t^2} = -\frac{1}{\rho c^2} \frac{\partial^2 R}{\partial z^2} , \qquad (10)$$

where we have dropped the subscripts on e; ρ is the crystal density and c the normal ultrasonic velocity. $R(=R_{zz})$ is the zz component of magnetoelastic stress and plays an analogous role to the polarization in the electromagnetic propagation problem,[10]

$$R = N \,\mathrm{Tr}\left(+\frac{\partial \mathcal{H}_c}{\partial e}\,\sigma\right), \qquad (11)$$

where σ is the density matrix in the laboratory frame and $\sigma' = U^\dagger \sigma U$ is the transformed density matrix. N is the total spin population.

We now specialize to the $\Delta\langle S_z\rangle = \pm 2$ transition, letting $2\mu = \omega$ and neglecting matrix elements of $\|\mathcal{H}'\|$ which are rapidly oscillating with frequencies of order $\frac{1}{2}\omega$. In terms of the elements of the density matrix defined,

$$V = iN\sigma'_{ca} e^{-i[kz + \phi(z)]} + \text{c.c.} ,$$

$$U = N\sigma'_{ca} e^{-i[kz + \phi(z)]} + \text{c.c.} , \qquad (12)$$

$$W = N(\sigma'_{cc} - \sigma'_{aa}) ;$$

$W = (N_c - N_a)$ where N_c, N_a are the population densities of the $\langle S_z\rangle = +1$, -1 states, respectively.[11] The equation of motion for σ' is

$$i\hbar\dot{\sigma}' = [\mathcal{H}', \sigma'] + \text{damping}. \qquad (13)$$

The damping terms are of two types: spin-lattice relaxation with time constant T_1 and spin-spin re-

laxation with time constant T_s. Then T_1 is the damping time for diagonal elements of σ', and the damping time for off-diagonal elements is $T_2 \approx (1/T_s + 1/T_1)^{-1}$. The equations for $\dot{v}'_{ab}, \dot{v}'_{bc}, \dot{v}'_{bb}$ do not involve U, V, W, and vice versa except through spin-lattice relaxation.[12] For very low intensities which do not materially alter the relative spin populations of the states, or for pulse lengths which are short compared with T_1, the coupled equations for $\dot{U}$, $\dot{V}$, $\dot{W}$ may be considered separately from the others. Then,

$$\frac{dU}{dt} = -V\Delta\omega - \frac{U}{T_2}\ , \quad \frac{dV}{dt} = +U\Delta\omega - 2\kappa\mathcal{E}W - \frac{V}{T_2}\ ,$$

$$\frac{dW}{dt} = 2\kappa V\mathcal{E} - \frac{W - W_0}{T_1}\ , \tag{14}$$

$$\kappa = \kappa_2 = (3/4\hbar)\,G_{11}\sin^2\Theta,\quad \Delta\omega = \omega_0 - \omega,\quad \omega_0 = (\omega_c - \omega_a),$$

and W_0 is the initial (i.e., $\tau = -\infty$) equilibrium value of W.

Let

$$R(\Delta\omega, z, t) = R_+(\Delta\omega, z, t)\, e^{i[\omega t - kz - \phi(z)]} + \text{c.c.},$$

with R_+ slowly varying in the same sense as $\mathcal{E}$. From Eqs. (11) and (12)

$$R_+(\Delta\omega, z, t) = +\tfrac{1}{2}\hbar\kappa[U(\Delta\omega, z, t) + iV(\Delta\omega, z, t)]\ . \tag{15}$$

Our problem is now identical with the two-level system coupled to an electromagnetic field except for the spatial (rather than temporal) derivative appearing in the inhomogeneous term in the acoustic wave equation (10). This is characteristic of all acoustic driving forces.[13] It leads to a dispersion relation for APR, which is derived in the Appendix, and which differs from that for electromagnetic resonance. However, in the slowly varying envelope approximation, used in MH, the difference vanishes.

Following MH we describe the random distribution of resonant frequencies by a normalized distribution function $g(\Delta\omega)$,

$$R_+(z,t) = \int_{-\infty}^{\infty} g(\Delta\omega) R_+(\Delta\omega, z, t) \times e^{i[\omega t - kz - \phi(z)]}\, d(\Delta\omega)\ . \tag{16}$$

Then, in the slowly varying envelope approximation, Eq. (10) reduces to

$$\frac{\partial\mathcal{E}}{\partial z} = -\frac{1}{c}\frac{\partial\mathcal{E}}{\partial t} - \frac{\hbar\kappa\omega}{4\rho c^3}\int_{-\infty}^{\infty} V(\Delta\omega, z, t) g(\Delta\omega)\, d(\Delta\omega)\ , \tag{17}$$

$$\frac{\partial\phi}{\partial z}\,\mathcal{E} = -\frac{\hbar\kappa\omega}{4\rho c^3}\int_{-\infty}^{\infty} U(\Delta\omega, z, t) g(\Delta\omega)\, d(\Delta\omega). \tag{18}$$

Equations (17) and (18) are the acoustic analogs of Eqs. (22) and (23) in MH. From them, together with Eqs. (14), all the results derived in MH follow, under the same approximations as made there.[14]

The Beer's law absorption constant for large inhomogeneous broadening is (see Appendix)

$$\alpha_0(\Delta\omega) = \pi\hbar n\kappa^2\omega g(\Delta\omega)/\rho c^3\ ,$$

where $n = -W_0$, positive in equilibrium. [Hereafter, α_0 will be written without the argument to designate $\alpha_0(0)$.]

B. Application to Ni^{2+} and Fe^{2+} in MgO

Effect of $\mathcal{H}_{SL}$. Rhodes, Szöke, and Javan[7] have shown that SIT is seriously modified if there are transitions with overlapping frequencies and differing matrix elements. The precession rate about the driving field in the rotating frame is $2\kappa\mathcal{E}$ for those transitions in resonance at frequency ω. Thus if there are differing values of κ among the various spins, reversible dephasing results. This occurs in our case if we allow for mixing of the Zeeman wave functions by off-diagonal matrix elements of $\mathcal{H}_{SL}$, since these are proportional to the randomly distributed static strains which vary from site to site. The perturbed wave functions, to first order in $\mathcal{H}_{SL}/\hbar\omega$, at a given spin site, are

$$\psi_+ = \psi_c + \frac{\underline{D}}{\hbar\omega_0}\,\psi_a + 2\,\frac{\underline{E} + \underline{D}}{\hbar\omega_c}\,\psi_b\ ,$$

$$\psi_0 = \psi_b + 2\,\frac{\underline{E} - \underline{D}}{\hbar\omega_a}\,\psi_a - 2\,\frac{\underline{E} + \underline{D}}{\hbar\omega_c}\,\psi_c\ , \tag{19}$$

$$\psi_- = \psi_a - \frac{\underline{D}}{\hbar\omega_0}\,\psi_c - 2\,\frac{\underline{E} - \underline{D}}{\hbar\omega_a}\,\psi_b\ ,$$

where $\underline{E}$ and $\underline{D}$ are matrix elements of the first and second terms, respectively, of $\mathcal{H}_{SL}$, Eq. (2).

We now have to consider the effects on κ_1 and κ_2 of transition operators of $\mathcal{H}_c$ of the form $d_{x'x'}S^2_{x'}$, $d_{z'z'}S^2_{z'}$, $d_{x'z'}(S_{x'}S_{z'} + S_{z'}S_{x'})$, and those which were entirely omitted earlier, $\gamma H\epsilon_{z'x'}S_{x'}$ and $\gamma H\epsilon_{z'z'}S_{z'}$. The additions to κ_2 due to all such operators are of second or higher order in $\vec{\mathrm{E}}/\hbar\omega$ and $\vec{\mathrm{D}}/\hbar\omega$ except for the following:

$$\Delta\kappa_2 \approx -2\kappa_1(\underline{E}/\hbar\omega_0) + 2\gamma H F_{11}(\underline{D}/\hbar\omega_0) \times (\sin 2\Theta - \cos 2\Theta). \tag{20}$$

F_{11} (in Voigt notation) is a tensor element of $\overleftrightarrow{\mathrm{F}}$,

$$\epsilon_{ij} = \sum_{kl} F_{ijkl}\, e_{kl}\ . \tag{21}$$

Additions to κ_1 are similar except there are also added terms proportional to $\gamma H F_{IJ}$ and independent

of $\underline{D}$ and $\underline{E}$.

The tensors $\underline{\underline{D}}$ and $\underline{\underline{E}}$ have the same form as $\underline{\underline{d}}$ and $\underline{\underline{\epsilon}}$ but with the random static strains replacing the ultrasonic strain. Thus the average value of $\underline{D}$ is proportional to an average of $(\underline{\underline{G}})\cdot$(static strain) and the averaged $\underline{E}$ is proportional to $(\hbar\gamma H\underline{\underline{F}})\cdot$(static strain). In Table I are listed values of $\underline{\underline{F}}$ and $\underline{\underline{G}}$ for Ni^{2+} and Fe^{2+} in MgO, as well as $T_{21}^{*}=\pi g_1(0)$, which is a measure of the width of the inhomogeneous broadening of the $\Delta\langle S_z\rangle=1$ transitions. With

$$\omega_0=2\gamma H\approx 2\pi\times 10^{10}\ \text{sec}^{-1},$$

$\underline{E}/\underline{D}\approx 0.1$ for Fe^{2+}. Thus the dominant broadening of the $\Delta\langle S_z\rangle=1$ transitions, which is first order in $\underline{E}$ and $\underline{D}$, is primarily due to $\underline{D}$ terms and we may take $\hbar T_{21}^{*-1}\approx \underline{D}_{av}$. Then, since κ_1 and κ_2 are both proportional to G_{11}, the fractional deviation in κ_2 at $\Theta=90^\circ$ is, from Eq. (20),

$$\Delta\kappa_2/\kappa_2\approx(\underline{E}/\underline{D})(\omega_0 T_{21}^{*})^{-1}<0.004$$

for Fe^{2+}. The elements of $\underline{\underline{F}}$ are unknown for Ni^{2+} but are presumably smaller than those of $\underline{\underline{G}}$. Since $(\omega_0 T_{21}^{*})^{-1}$ is a factor ≈ 10 smaller, $\Delta\kappa_2/\kappa_2$ is no larger than for Fe^{2+}. Reversible dephasing effects should, therefore, be unimportant for total turning angles (pulse areas),

$$\theta(z)=2\kappa\int_{-\infty}^{\infty}\mathcal{E}(z,t)\,dt<250\pi \qquad (22)$$

at $\Theta=90^\circ$. This inequality holds in our experiments, except perhaps at the very highest input intensities on the Fe^{2+} transitions. It should be noted, however, that for small Θ, $\Delta\kappa$ and κ can be of the same order because of their different angular variations.

Owing to the additional terms in $\Delta\kappa_1$, the fractional deviation is of order $(\underline{E}/\underline{D})$, ≈ 0.1 for Fe^{2+}. Therefore, on the $\Delta\langle S_z\rangle=1$ transitions, dephasing can result for $\theta>10\pi$.

Numerical computations for Ni^{2+}. The principal theoretical results given in MH assume infinite T_1 and T_2 and zero nonresonant background loss. These conditions do not obtain in our experiments. Furthermore, the theory of MH applies to unidirectional propagation through the resonant medium, whereas our measurements were conducted on pulses

TABLE I. Spin-lattice coupling parameters (per unit strain) for Ni^{2+} and Fe^{2+} in MgO.

	F_{11} [a]	F_{44} [a]	G_{11} [b] (cm^{-1})	G_{44} [b] (cm^{-1})	T_{21}^{*} (sec)
Fe^{2+}	−145	−40	+725	+460	2×10^{-10}
Ni^{2+}	...	...	+57	+43	10^{-9}

[a] T. G. Phillips and R. L. White, Phys. Rev. 153, 616 (1967).

[b] Averaged values from G. D. Watkins and E. Feher, Bull. Am. Phys. Soc. 78, 29 (1962); N. S. Shiren, *ibid.* 78, 29 (1962).

TABLE II. Parameters utilized in the round-trip calculation.

$\alpha_0 L$	$\alpha_s L$	T_2 (sec)	T_2^{*} (sec)	T_1 (sec)	τ_0 (sec)
10	1.6	1.2×10^{-6}	2×10^{-8}	4×10^{-4}	3×10^{-7}

which were reflected back through the host absorber after having already traversed it once. Since there is also a reflection at the transducer-MgO bonding interface, standing-wave regions are set up at both ends.

Hopf's calculation[6] approximates this case, neglecting standing waves; i.e., it was assumed that the reflection occurred at a surface placed further away by a distance greater than half the maximum pulse width. The parameters used are listed in Table II; they are the same as those prevailing in some of the experimental runs on Ni^{2+}. α_s is the decay constant for nonresonant absorption in the host crystal, and L is the propagation path length (twice the length of the MgO rod). The input pulse envelope was taken as

$$\mathcal{E}(0,t)=\mathcal{E}_0\sin^2(\pi t/2\tau_0),\quad 0\le\tau/2\tau_0\le 1. \qquad (23)$$

$\tau_0\equiv\tau_H(0)$, where $\tau_H(z)$ is the full pulse width at half-amplitude at z. For this shape pulse $\tau_0=0.3$ μsec corresponds to a base width of 0.6 μsec, which is approximately the experimental value.

The results of the calculation are shown in Figs. 1–3 for both a single pass and a round trip with reflection. The pulse energy per cm^2 is

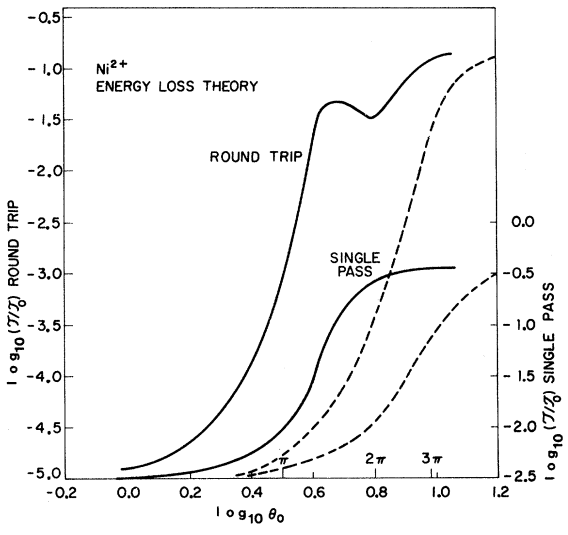

FIG. 1. Energy-loss computations in SIT (solid lines) for the parameters listed in Table II, and in saturation (dashed lines) for the same parameters except T_2.

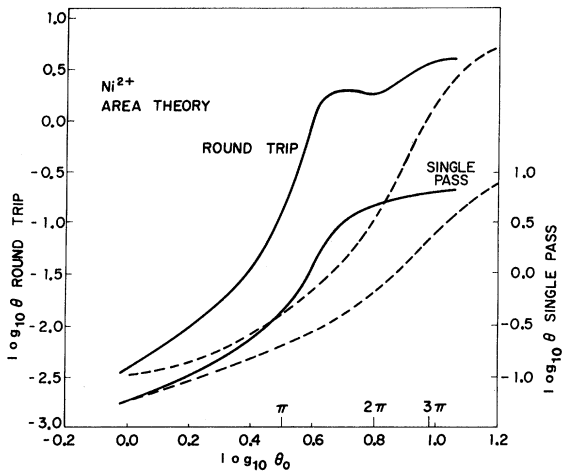

FIG. 2. Area computations in SIT (solid lines) for the parameters listed in Table II, and in saturation (dashed lines) for the same parameters except T_2.

$$\mathcal{T}(z) = 2\rho c^3 \int_{-\infty}^{\infty} \mathcal{E}^2(z,t)\, dt\,,$$

and $\mathcal{T}_0 \equiv \mathcal{T}(0)$. $\theta_0 \equiv \theta(0)$ is the value of $\theta(z)$ [defined through Eq. (22)] at the entry plane. Figure 1 shows the rapid decrease in fractional energy loss as θ_0 (or input power) is increased. (Of course, $\mathcal{T}/\mathcal{T}_0$ can never be greater than $e^{-\alpha_s L}$ for the round trip, and $e^{-\alpha_s L/2}$ for the single pass.) The effect may also be seen in Fig. 2 where $\theta(L)$ and $\theta(\frac{1}{2}L)$ are plotted against θ_0. An interesting feature of the round-trip curves, in both figures, is the single oscillation near the upper ends. The energy loss goes through a minimum near $\theta_0 = 1.6\pi$, while the pulse area goes through a small stable (or steady-state) region in the same vicinity.

In Fig. 3 the theoretical results for $\tau_H(L)$ and $\tau_H(\frac{1}{2}L)$ and the delay time at the peak of the pulse, DT, are shown. The roughly bell-shaped behavior, characteristic of the coherent interaction, has been derived previously by Hopf and Scully[5] for the ideal SIT case of MH.

The area theorem derived in MH is an exact analytic expression for $d\theta/dz$ under the conditions: $\alpha_s = 0$; T_2, $T_1 \to \infty$; $\tau_H \gg T_2^*$. Following the same mathematical procedure, starting from Eqs. (17) and (14) [with the addition of a term $-\frac{1}{2}\alpha_s \mathcal{E}(z,t)$ on the right-hand side of Eq. (17)], an analytic form may also be deduced without the restriction $\alpha_s = 0$,[15]

$$\frac{d\theta}{dz} = -\tfrac{1}{2}\alpha_0 \sin\theta - \tfrac{1}{2}\alpha_s \theta\,. \qquad (24)$$

It is a remarkable fact, and perhaps fortuitous, that Eq. (24), which is derived for unidirectional propagation neglecting relaxation, predicts many of the results found in the full round-trip computation.

Steady-state solutions of Eq. (24) occur at values of θ for which the right-hand side vanishes, and therefore only if $(\alpha_s/\alpha_0) \leq \frac{2}{3}\pi$. There are two types, with M an integer they are $(2M-1)\pi \leq \theta_1 \leq (2M-\frac{1}{2})\pi$ (odd π solutions in MH) and $(2M-\frac{1}{2})\pi \leq \theta_2 \leq 2M\pi$ (even π solutions in MH). Only the latter, however, are stable against small changes in θ_0; i.e., in a region about $\theta_0 = \theta_2$, θ is stationary with respect to θ_0. With the parameters in Table II, Eq. (24) has only two solutions: $\theta_1 = 1.2\pi$, $\theta_2 = 1.7\pi$. The agreement of the latter with the value $\theta_0 = 1.6\pi$ from the full computation, Fig. 2, is thus very good. By analogy with the 2π solution in MH, an energy-loss minimum should also occur near $\theta_0 = \theta_2$. The exact position depends on initial pulse shape and moves to slightly smaller values of θ_0 for input pulses which do not have the final steady-state shape. Thus there is also approximate agreement with the energy-loss computation, Fig. 1. There is disagreement, however, in the sense that θ_2 from Eq. (24) is a steady-state solution $\theta \to \theta_2$, whereas in Fig. 2 the stable value of θ, near $\theta_0 = \theta_2$, is $\approx 0.64\pi$. This may be due to the effect of T_2, which is not included in Eq. (24).

This analysis might be expected to agree even more closely with the single-pass computations. Since the latter do not exhibit a stationary θ, agreement with the double-pass results may be fortuitous. On the other hand, at $\theta_0 = \theta_1$, both the single- and

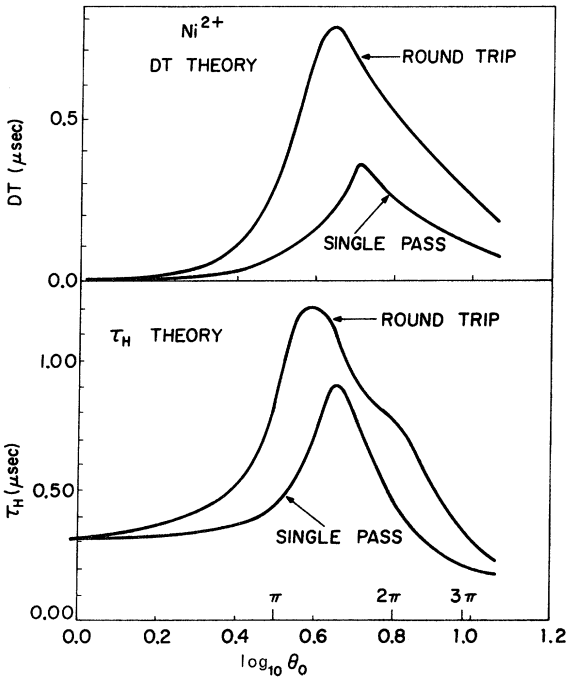

FIG. 3. Computed delay times (above) and pulse widths (below) in SIT for the parameters listed in Table II.

double-pass results in Fig. 2 have the same final area $\theta \approx 0.32\pi$ which is, therefore, a steady-state area. Thus, at least empirically, Eq. (24) gives the correct θ_0 ($=\theta_1$) from which the nonstationary steady-state develops with $\theta < \theta_1$ due to the presence of finite T_2. Further evidence for the validity of this conclusion is provided by an argument due to Hopf and Scully[5] which shows that the maximum τ_H should occur when the pulse is propagating in the above state, i.e., for $\theta_0 = \theta_1$, and this is exactly where the peak of the round-trip curve for τ_H lies in Fig. 3. To the extent that this solution is similar to the π solution in the ideal case, the maximum value of $\underline{DT}$ should occur at θ_0 slightly greater than θ_1. This is also shown in Fig. 3 where the maximum $\underline{DT}$ is at $\theta_0 \approx 1.4\pi$.

Comparison with saturation. In the opposite limit on T_2 to that prevailing in ideal SIT, i.e., for $\tau_0 \gg T_2$, saturation of the resonant system becomes important at high-input intensities. This is also characterized by a rapid decrease in the fractional energy loss as input power is increased. Since our experiments on Ni^{2+} and the theoretical calculation by Hopf lie between the two limiting cases, we have investigated the behavior of the pulse energy and area utilizing the parameters in Table II but with the assumption $T_1 \gg \tau_H \gg T_2 \gg T_2^*$.

Expressions for the radiation intensity and population density under pulse saturation conditions have been derived by several authors,[16,17] starting from Eq. (17) and the steady-state solutions to Eqs. (14) (see Appendix). When nonresonant host absorption is included in Eq. (17) the solutions must be evaluated numerically. Results of such computations are shown in Figs. 1 and 2 for both the single and double passes. Except for the structure in the double-pass SIT curves, the shapes of the saturation curves are very similar to those of the analogous SIT solutions. Saturation sets in at larger θ_0 than does SIT, but the rate at which the energy loss decreases is about the same.

This result is not restricted to the present problem as may be seen by comparing ideal SIT with the saturation solutions given in Refs. 16 and 17. Their expression for the radiation intensity may be written in terms of θ_0,

$$\mathcal{E}^2(z,t) = [\mathcal{E}(0, t - z/c)]^2 \times [1 - (1 - e^{\alpha_0 z}) e^{-T_2^* \theta_0^2 b(z,t)/\tau}]^{-1}, \qquad (25)$$

where

$$b(z,t) = \int_{-\infty}^{t-z/c} f^2(t)\, dt \Big/ \int_{-\infty}^{\infty} f(t)\, dt$$

and $f(t)$ is a shape function, of unity peak amplitude, such that

$$\theta_0/\kappa = 2\int_{-\infty}^{\infty} \mathcal{E}_0 f(t)\, dt = 2\mathcal{E}_0 \tau .$$

In general, $b(z, t)$ is less than or of order unity. [With $f(t)$ from Eq. (23), $\tau = \tau_0$ and $b(z,\infty) = \frac{3}{4}$.] For large $\alpha_0 z$, Eq. (25) shows that the apparent attenuation constant is reduced to $\frac{1}{2}\alpha_0 z$ at $\theta_0^2 = \frac{1}{2}\alpha_0 z\tau/T_2^*$, while $\mathcal{T} \approx \mathcal{T}_0$ at $\theta_0^2 \sim 2\alpha_0 z\tau/T_2^*$. In ideal SIT these points occur with the same relative values of θ_0; i.e., at $\theta_0 = \pi$ and $\theta_0 = 2\pi$, respectively. Therefore, observation of the rapid decrease of apparent absorption with increasing power does not, by itself, establish the presence of SIT unless absolute (not relative) values of θ_0 can be ascertained, or it is known from other measurements that $\tau \ll T_2$.

Coherence effects are most clearly differentiated from saturation by measurements of DT and τ_H as functions of θ_0 and by observation of pulse shapes. Whereas in saturation the pulse shape becomes asymmetric,[16] peaking toward the back of the pulse, in SIT it tends to become symmetric. Also, although there can be an apparent delay of the peak in saturation, it cannot be greater than the initial pulse width.[18] The most outstanding qualitative difference, however, is that in transparency the pulse width increases to a value $> \tau_0$ and then narrows as θ_0 is increased; in saturation τ_H is always less than or equal to τ_0.

III. EXPERIMENTAL METHOD

All measurements were made at frequencies ≈ 9 GHz using the pulse-echo technique. 2J51 magnetrons were used to generate rf pulses whose base widths could be adjusted in the range 0.6–3 μsec. The shapes and τ_H of the pulses were different for different magnetrons. Only longitudinal waves propagating on ⟨100⟩ axes of the MgO were utilized, although similar effects were observed on other axes and with transverse polarizations.

In the earlier experiments,[1] the pulse shapes were distorted by high Q cavities and narrow-band detection methods. Therefore, in the work reported here, the cavity Q was intentionally reduced to approximately 800, and a super heterodyne receiver with an i.f. bandwidth of 100 MHz centered at 250 MHz was utilized. Otherwise, the ultrasonic drive cavity and crystal arrangement were similar to those used previously. Quartz transducers were bonded to MgO crystals having optically flat, polished, and parallel faces. Both quartz and MgO were 1–2 cm long and 3 mm in diam. Although it would appear desirable to have made single-pass measurements instead, utilizing thin evaporated transducers, this would not have averted the presence of standing waves at both ends of the MgO. Also, the quartz transducer acted as a buffer to remove the MgO far enough away from

the cavity so that rf leakage did not induce spin-resonance transitions.

Measurements were made on two crystals (samples 1 and 2) containing Ni^{2+} impurities, and one (sample 3) with Fe^{2+}. Samples 1 and 2 were cut from the same boule and, presumably, the only differences are the lengths. Their relevant parameters are listed in Table III. For sample 1, $\alpha_0 L$ at 4.2 °K was measured directly at $\Theta = 90°$ and checked against measurements at other values of Θ. For sample 2, the 90° value was extrapolated from measurements at smaller angles, since $\alpha_0 L = 8$ was the largest absorption for which the signal-to-noise ratio at low-input powers (i.e., in the linear absorption range) was great enough to allow accurate attenuation measurements. The absorption constant of the Fe^{2+} transition in sample 3 was obtained by a method based on the suppression of second harmonic generation by paramagnetic resonance dispersion and absorption.[19] The 1.8 °K, $\Theta = 90°$ values were calculated from those at 4.2 °K using the appropriate Boltzmann factors, and also checked against measurements at smaller Θ.

The value, $\alpha_s L = 1.6$, for sample 1 was taken from one particular experiment in which four successive echoes in the MgO were exponentially related (Sec. IV, Fig. 12), and the value for sample 2 is 1.6 times the ratio of the sample lengths. Generally in microwave ultrasonic experiments, successive echoes show nonexponential modulation due to nonparallelism of the reflecting surfaces and/or wedge-shaped bonds. An observed exponential pattern can thus be coincidental, not representing the true α_s. The quoted value above should be considered an upper limit and therefore represents a possible source of error in comparing experiment with Hopf's computations.

The values of T_2, given in Table III, were measured by rf spin-echo methods at 9 GHz on the $\Delta\langle S_z\rangle = 1$ transitions. If T_2 were dominated by spin-spin interactions then the values for $\Delta\langle S_z\rangle = 2$ transitions should theoretically be smaller than the measured ones by a factor 0.82.[20] However, the strong temperature dependence is an indication that spin-lattice relaxation is of at least equal importance, and then T_2 should be slightly larger for $\Delta\langle S_z\rangle = 2$ than for $\Delta\langle S_z\rangle = 1$ at the same transition frequency.[12]

Data were taken only on the $\Delta\langle S_z\rangle = 2$ transitions. The effect is qualitatively similar on the $\Delta\langle S_z\rangle = 1$ transitions, but measurements at high-power levels are complicated by the presence of a double quantum transition which itself exhibits SIT effects. Also, reversible dephasing is expected to be more important for $\Delta\langle S_z\rangle = 1$.

Figure 4 shows oscilloscope traces taken on the Ni^{2+} line at 1.8 °K, for three input pulse widths, as the magnetic field is varied through resonance. Figure 5 illustrates the effects observed on Ni^{2+} at 4.2 °K as a function of input power. The presence of a threshold and the pronounced tendency of the pulse to assume a smooth symmetric shape as well as the concomitant decrease in velocity (pulse delay) and changes in τ_H are clearly evident, particularly for the shorter input pulses. The 2.3-μsec pulse, in Fig. 5(c), exhibits typical saturation behavior primarily,[16,17] with only slight coherence broadening. The ragged appearance of the short pulses in Fig. 5(a), at low powers, is probably due to a small amount of frequency modulation in this particular magnetron. (Pulses from other magnetrons did not exhibit such behavior.) In the linear region the absorption therefore varies in time. However, in the nonlinear region of SIT it is seen that the reshaped pulse stabilizes against this modulation.

Figure 5 is also illustrative of the type of data from which quantitative values of $\theta, \mathcal{T}$, DT, and τ_H were extracted. Each trace is a multiple expo-

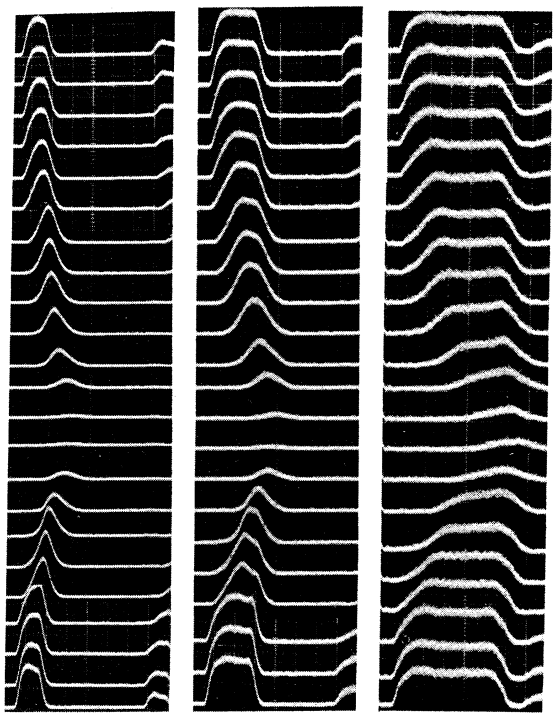

FIG. 4. Oscilloscope traces showing changes in pulse shape and delay as magnetic field is scanned (increasing from top to bottom) across Ni^{2+} transition in MgO sample 2 at 1.8 °K. Three input pulse widths are shown from left to right; $\tau_H(0) = 0.45$, 0.9, and 2.1 μsec. Time increases from left to right in each trace. A second round-trip echo may be seen on some traces. Off-resonance pulses shown at bottom of each set.

TABLE III. Parameters of the relevant Ni^{2+} or Fe^{2+} transitions in the various MgO samples. L is twice the sample length and t_L is the round-trip time off-resonance.

	Sample No. 1	Sample No. 2	Sample No. 3
L (cm)	1.82	2.37	2.18
t_L (sec)	1.97×10^{-6}	2.56×10^{-6}	2.35×10^{-6}
$\alpha_s L$	1.6	2.08	...
$\alpha_0 L$ (4.2 °K)	7.7 ± 0.3	10 ± 0.5	40 ± 4
(1.8 °K)	18 ± 1	23.4 ± 1.5	94 ± 10
T_2 (sec) (4.2 °K)	$(0.76\pm0.05)\times10^{-6}$	$(0.76\pm0.05)\times10^{-6}$	$(5.8\pm0.1)\times10^{-6}$
(1.8 °K)	$(1.20\pm0.05)\times10^{-6}$	$(1.20\pm0.05)\times10^{-6}$	$(11.0\pm0.2)\times10^{-6}$
T_2^* (sec)	2.3×10^{-8}	2.3×10^{-8}	3×10^{-9}
T_1T (sec °K)	9×10^{-3}	9×10^{-3}	10^{-4}

sure of about 100 repetitive pulses. The i.f. gain was adjusted to compensate the change in input power in order, insofar as possible, to maintain an approximately constant peak input to the second detector. Amplitude measurements were made at 0.02-μsec intervals along the traces. These plus the i.f. and rf attenuator readings were entered into a computer program which adjusted for detector nonlinearity and reduced the data. DT is the time delay measured at the peak of the pulses from the peak of the off-resonance pulse. Where the latter had no pronounced peak the midpoint ($\frac{1}{2}\tau_0$) was taken as a fiducial mark. $\tau_H = \tau_H(L)$ was measured, according to its definition, at the half-amplitude points.

The magnitudes of the errors in the reduced data were determined from repeated measurements made on one experimental run. They are indicated in Fig. 7, and are assumed to apply to all other sets of data at equivalent ordinate and abscissa values.

In the Ni^{2+} experiments, absolute values of θ and θ_0 were determined by equating

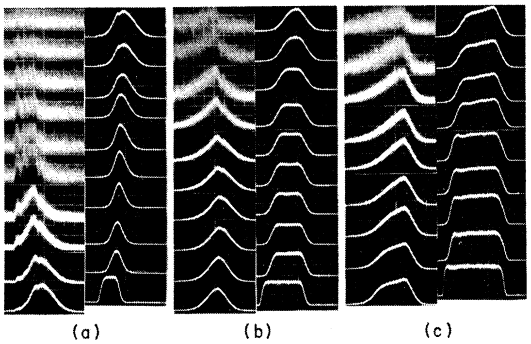

FIG. 5. Oscilloscope traces showing changes in pulse shape and delay as input power is increased (top to bottom in each column). Ni^{2+} resonance in MgO sample 1 at 4.2 °K, $\tau_H(0)$ = (a): 0.4 μsec, (b): 0.87 μsec, (c): 2.3 μsec. Where possible, detector gain was adjusted to keep output amplitudes constant. Off-resonance pulses shown at bottom right of each set.

$$2\kappa\int_{-\infty}^{\infty}\mathcal{E}(0,\ t)\,dt$$

at the maximum τ_H (measured with the shortest pulse inputs) to the θ_1 solution of Eq. (24). This method has little theoretical basis other than the agreement with Hopf's calculation, as discussed in Sec. II. However, the long pulse data of Fig. 5, which shows the qualitative effects expected under saturation conditions for a pulse width greater than T_2, is in almost perfect quantitative agreement with saturation calculations when θ and θ_0 are calibrated as above, from the 0.4-μsec data. In addition, $\mathcal{E}_0$ determined in this way is within a factor 2 of the best strain calibrations we were able to make from input rf power measurements and conversion efficiencies.

In the neighborhood of the steady-state solution θ_1, the absorption can be large (Fig. 1), also τ_H increases with increasing α_0,[5] thereby decreasing the pulse intensity for a given θ. Consequently, with $\alpha_0 L > 13$ in the Ni^{2+} measurements, the pulse was not observable above the noise at the peak τ_H or DT values, and it was not possible to make an absolute calibration of θ or θ_0. In Fe^{2+} experiments such measurements were even less tractable because, in addition to larger α_0, a given minimum detectable intensity corresponds to a value of θ larger by the ratio of the κ's (≈ 12.5). Efforts to take data on Fe^{2+} at Θ values small enough to obviate this problem were unsuccessful, probably because of the relatively large mixing of the wave functions which occurs at small angles (see Sec. II). Under these conditions saturation behavior only was observed, presumably of the type termed "effective" saturation by Rhodes and Szöke.[21]

IV. RESULTS

A. Ni^{2+}

Pulse shapes. A principal result of the theory in MH is the hyperbolic secant-shape of the steady-state 2π pulse. It is clear from Figs. 4 and 5 that in our experiments, also, the pulse is reshaped in

the regions of large delay, tending toward a symmetric bell shape. In Fig. 6 we have compared three representative pulses from one of the Ni^{2+} runs with least-squares-fitted sech and Gaussian shapes. The Gaussian is an excellent fit (least-squares error < 0.01), while the sech does not fit as well in the wings. This is to be expected, even in ideal transparency, when the transmission path length is finite. The wings must then cut off more sharply than in the true steady state, attained in the limit $t \to \infty$.

Double-pass results. Data taken on sample 1 at 1.8 °K are presented in Fig. 7. With the exception $\tau_0 = 0.45$ μsec, all the parameters are identical with those used in Hopf's computation. The results of the latter for θ and $\mathcal{T}/\mathcal{T}_0$ are also shown for comparison. (Note that in all the figures the logarithms are $\log_{10}$.) Assuming that the area calibrations are correct, the experimental points fit the SIT theory fairly well except that the structure associated with formation of a steady state is much smaller and within the experimental error. [The decrease in $\mathcal{T}/\mathcal{T}_0$ beyond $\theta_0 \approx 3\pi$ is due to the onset of second harmonic generation[22] (due to lattice anharmonicity) which is not completely suppressed by the resonance.] On the other hand, if the calibrated values of θ and θ_0 were too small, by a factor 2,

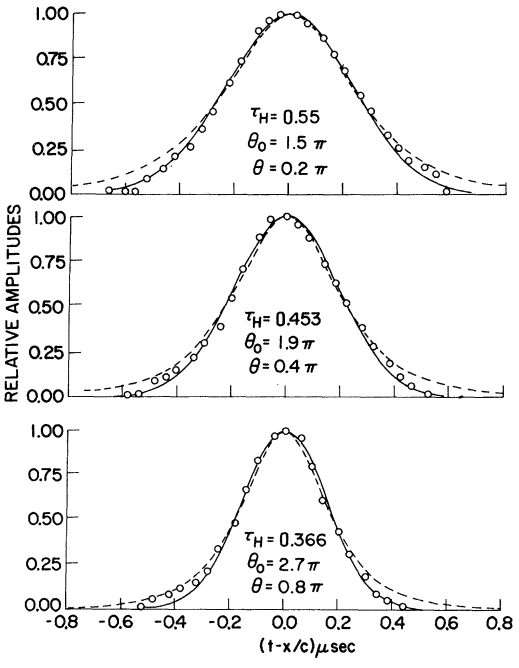

FIG. 6. Measured pulse shapes (circles) and least-squares-fitted Gaussian (solid lines) and hyperbolic secant (dashed lines) curves for three input areas. Ni^{2+} resonance at 4.2 °K. $\tau_H(0) = 0.4$ μsec.

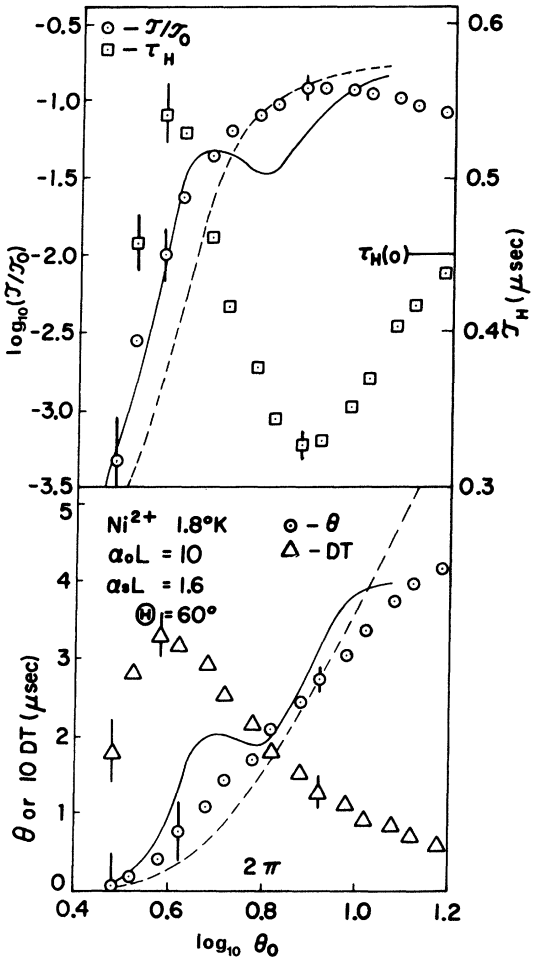

FIG. 7. Measurements on sample 1 for the parameters shown, and computed curves from Figs. 1 and 2. For the saturation (dashed) curves θ and θ_0 twice as large as indicated. Energy and pulse width shown above. Area and pulse delay shown below.

then the data would fit the saturation theory more closely. This is shown by the saturation curves in Fig. 7 which were evaluated for areas twice as large as indicated by the ordinate and abscissa.

As expected from the discussion in Sec. II, the θ and $\mathcal{T}$ data only distinguish between saturation and transparency to the extent that the area calibrations are correct. However, the experimental values of DT and τ_H clearly illustrate the typical coherence behavior shown in Fig. 3. The sharp rise and slower fall is particularly evident in the delay-time data. Quantitative agreement is not as good; the maximum in DT and τ_H, in Fig. 7, are smaller than theory by a factor ≈ 2, and the narrowing is greater than predicted by theory. (The increase towards τ_0 at larger θ_0 is at least partially another manifestation of harmonic generation.)

Although the base width of the pulse was 0.6 μsec in both theory and experiment, the pulse shapes were such that the ratio of the experimental to theoretical τ_0 was ≈ 1.5. A larger experimental τ_0 can affect the comparison with theory in two ways: Saturation conditions are approached because the ratio T_2/τ_0 is smaller; to the extent that τ_H reflects τ_0, the standing-wave regions (neglected in the theory) are a larger fraction of the total propagation path.

Measurements on sample 2 at 4.2 °K are shown in Fig. 8. $\alpha_0 L$ was the same as in Fig. 7, T_2 was smaller, and τ_0 slightly larger. $\mathcal{T}$ and θ show less evidence of structure than at 1.8 °K and fit the displaced saturation curve better. However, this may not be entirely due to the shorter T_2; the smaller value of α_0 (not $\alpha_0 L$) causes the solutions θ_1 and θ_2 of Eq. (24) to be nearly degenerate, which tends to remove the extremum (stable θ region) in the transparency theory. (This argument applies to all the Ni^{2+} runs at 4.2 °K.) The maximum DT is smaller by a factor 1.2 which probably reflects the factor 1.5 decrease in T_2. The maximum τ_H is larger by considerably more than the increase in τ_0 but the total variation in τ_H is about the same as in Fig. 7.

Results on DT and τ_H are summarized in Table IV for six runs, comprising three values of $\alpha_0 L$ and two of T_2. τ_0 is also given. Runs 3 and 4 are those of Figs. 8 and 7, respectively. Runs 1 and 2 represent data from Figs. 5(a) and 5(b), respectively.

Comparing runs 1–5, it is seen that, in addition to the small increase in DT between runs 3 and 4 (mentioned above), the largest change occurs between 4 and 5, while DT is the same for 1 and 3. Thus an increase in $\alpha_0 L$ causes an increase in DT unless the latter is already limited by T_2. Comparison of runs 5 and 6 shows that with the longer T_2, DT is almost unaffected by a factor 2 increase in τ_0. The apparent increase in DT in run 2 over run 1 is a shift in the peak position due to saturation behavior (see below).

Similar behavior is exhibited by $\Delta\tau_H (= \tau_{H\,\max} - \tau_{H\,\min})$. $\tau_{H\,\max}$ also shows a similar variation with $\alpha_0 L$, but depends more directly on τ_0, as might be expected.

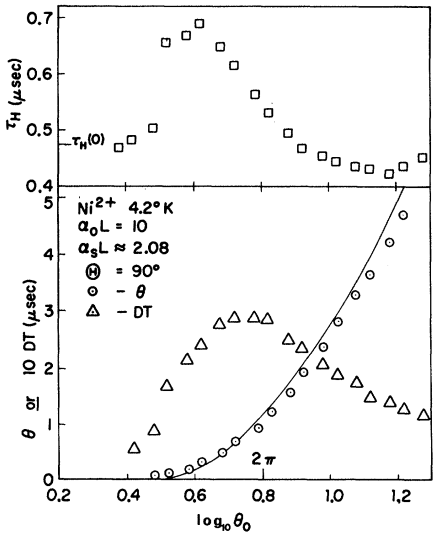

FIG. 8. Measurements on sample 2 for the parameters shown, and saturation curve computed for the same conditions but with θ and θ_0 twice as large as shown by the scales. Area and pulse delay shown below.

The effect of T_2 in limiting the maximum value of DT is illustrated more dramatically by Fig. 9, in which the DT line shape (at constant θ_0) from the 0.45-μsec data of Fig. 4 is plotted together with an attenuation line shape $\alpha_0(\Delta H)L$ measured in the linear absorption region at 4.2 °K (Θ adjusted for $\alpha_0 L = 8$). Since $\alpha_0 L = 23$ (for the DT data), the effect of α_s is small and $DT(\Delta H)$ should vary directly with α_0 (ΔH). [See MH and discussion above.] However, DT is relatively smaller, by a considerable factor, at the center than on the wings of the line, because the longer delays are more severely affected by small T_2.

Although the maxima of DT and τ_H are limited by T_2, their functional behavior with θ_0 does not appear to be changed from that theoretically predicted for coherence phenomena unless τ_0 is actually greater than T_2. This is illustrated by Fig. 10 which is a plot of τ_H for the 0.4- and 0.87-μsec data of sample 1 at 4.2 °K, pictured in Figs. 5(a) and 5(b). Al-

TABLE IV. Relevant parameters for six Ni^{2+} runs discussed in the text. All times are in μsec.

Run	$\alpha_0 L$	T_2	τ_0	$DT_{\max}$ (±0.02)	$(\tau_H)_{\max}$ (±0.01)	$(\tau_H)_{\min}$	$\Delta\tau_H$ (±0.02)
1	7.7	0.76	0.40	0.28	0.60	0.31	0.29
2	7.7	0.76	0.87	0.38	0.87	0.56	0.31
3	10	0.76	0.48	0.28	0.68	0.42	0.26
4	10	1.20	0.45	0.32	0.54	0.33	0.21
5	13	1.20	0.47	0.55	0.73	0.38	0.35
6	13	1.20	0.90	0.60	1.01	0.65	0.36

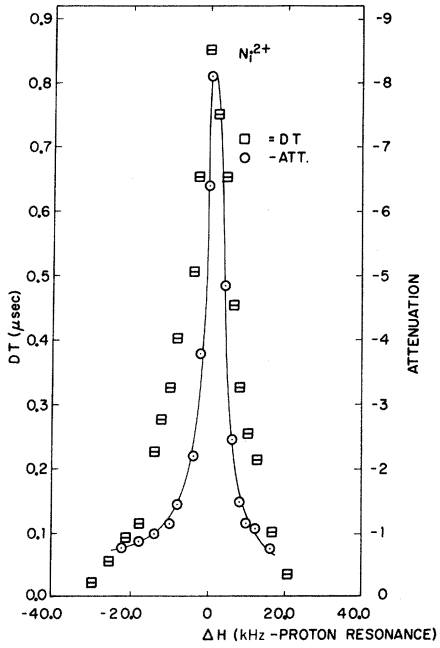

FIG. 9. Attenuation measured in the linear region for $\alpha_0 L = 8$, and pulse delay measured in SIT region for $\alpha_0 L = 23$, versus magnetic field. Solid line drawn through attenuation points.

though the $\tau_0 = 0.87$-μsec pulses show some qualitative manifestations of coherence effects, such as the formation of symmetric pulse shapes and apparent broadening in the tails, the quantitative data on τ_H exhibits the effects of saturation. τ_H is never larger than τ_0 for this set of data; it decreases monotonically with increasing θ_0 to a minimum value and then increases again towards τ_0. This is to be compared with the $\tau_0 = 0.4$-μsec behavior which is similar to that of Figs. 7 and 8. (Note that harmonic generation does not set in as early in Figs. 8 and 10 as in Fig. 7. This is because the intensity for a given θ_0 is smaller at $\Theta = 90°$ than at $\Theta = 60°$ by a factor $\frac{9}{16}$, due to the respective ratio of the κ's being $\frac{4}{3}$. For the 0.87-μsec data the intensity is additionally smaller by the ratio of τ_0^2, 0.21.)

In contrast, in run 6 with $\tau_0 = 0.9$ μsec but still smaller than T_2, $\tau_{H\,\max}$ is larger than τ_0. Also, in Fig. 4 it is seen that for both the 0.45- and 0.9-μsec inputs, at the maximum DT the pulse peak is delayed beyond the tail of the off-resonance pulse, whereas this is not true for the 2.1-μsec ($> T_2$) input. This again supports the general conclusion above; the effect on coherence behavior of increasing τ_0 is minimal until $\tau_0 > T_2$.

Multiple echoes. Figure 11 shows a sequence of four complete round-trip passes in the MgO off- and on-resonance. Energy and DT for several in-

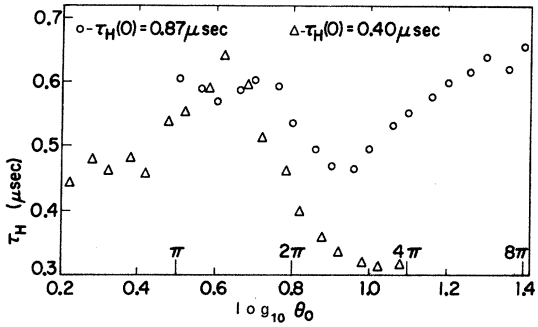

FIG. 10. Pulse width measurements from data of Figs. 5(a) and 5(b).

put power levels are plotted versus echo number in Fig. 12. The off-resonance data were used to evaluate $\alpha_s L$ as discussed in Sec. III. (In this connection we note that the transmission through the bonds is never better than ≈ 6 dB and is more usually ≈ 10 dB; the error in $\alpha_s L$ due to reflection losses is thus ≈ 0.1.) The outstanding features of these data are that, after the first round-trip echo, for each input power level the attenuation is constant; the delay time is linearly cumulative over the next three round trips, indicating a constant velocity; there is no further pronounced pulse reshaping. Also, at the higher-power levels the attenuation approaches α_s while the delay, although smaller, persists.

B. Fe^{2+}

In principle, Fe^{2+} is an almost ideal system for investigating SIT. The inhomogeneous broadening is large, very large α_0 can be attained, and T_2 at

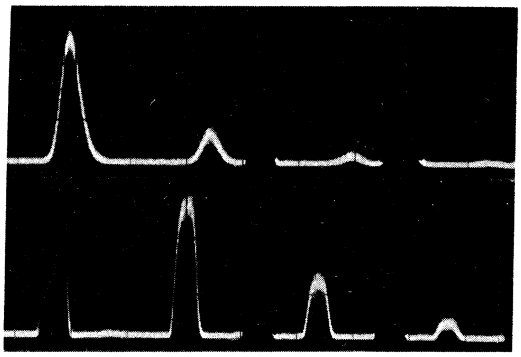

FIG. 11. Oscilloscope traces showing four complete round trips in the MgO. Time increases from left to right, 1 sec per division. Upper trace: ultrasonic frequency on Ni^{2+} resonance. Lower trace: off-resonance. Two echoes resulting from a round trip in the quartz transducer have been blocked out.

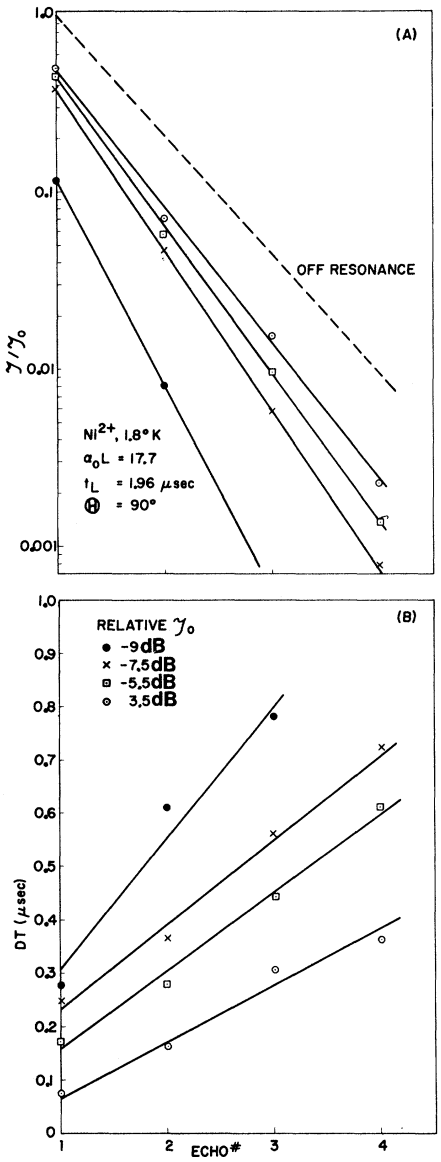

FIG. 12. Measurements on four successive round trips with the parameters shown. (A): Relative pulse energies. (B): Pulse delay times measured on each echo from its off-resonance position.

1.8 °K is an order of magnitude larger than both τ_0 and t_L. Also harmonic generation is less of a problem because of the lower intensity required for a given θ_0. However, the measurements were rendered extremely difficult by several factors and only qualitative results were obtained.

Even with spin concentrations of a few ppm the absorption is so large that it was not possible to make measurements at small θ_0, as explained in Sec. III. In addition, the pulse-echo amplitudes undergo severe modulation and distortion with variation in the magnetic field $\vec{H}$ as reported by several authors.[23–25] The origin of this effect is not completely understood and there may be several contributing causes.

Wigmore and Rosenberg[23] have offered an explanation based on phase interference among transmissions over multiple paths with differing concentrations. Combined with SIT delays, multipath propagation could lead to observation of multiple pulses, analogous to those seen in optical experiments, and caused there by filamentary transmission modes.[21] On the other hand, the author has observed that the modulation is a more rapid function of $\vec{H}$ if the transducer and MgO crystals are misaligned so that refraction occurs at the bonding surface, and this does not seem explainable by the above mechanism.

Coherence effects can partially explain the above phenomenon even without consideration of multiple paths. The results of computer calculations in MH show that pulses with $3\pi < \theta_0 < 5\pi$ approach a $\theta = 4\pi$ steady state which consists of two 2π pulses of unequal τ_H and correspondingly unequal DT. (Larger θ_0 pulses can similarly break up into three or more 2π pulses.)

Figure 13 is, the author believes, an example of such pulse "break up." As θ_0 increases the two pulses move closer together, in agreement with the theoretical results in MH. Both pulses have the characteristic bell shape and the DT's are in the same ratio as the τ's. The latter is not necessarily the case if break up is due to multiple-path transmission,

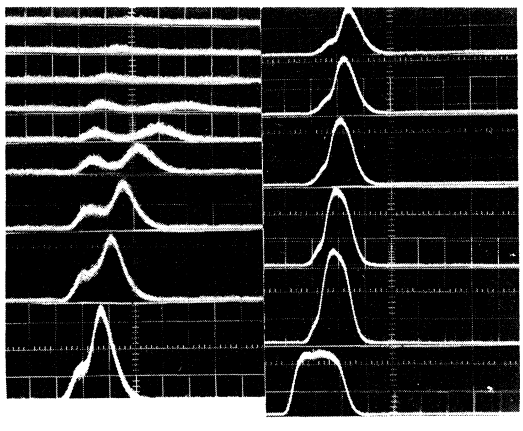

FIG. 13. Oscilloscope traces showing pulse break up due to interaction with Fe^{2+} resonance in MgO sample 3 with parameters given in Fig. 14. Input power increases from top to bottom in each column. Detector gain 8 dB higher on left than on right. Last trace shows off-resonance pulse at same input-power and gain settings as immediately preceding trace.

since then the α_0's can be different for the two paths. The smallest value of θ_0 at which the pulses can be seen must already be greater than 3π. For the reasons given earlier no absolute values of θ_0 could be ascertained, but comparison with the Ni^{2+} runs at the same input power levels indicates that the smallest θ_0 lies between 3π and 6π.

However, effects other than ideal SIT cannot be definitely ruled out. The ratio of the area of the second pulse to that of the first increases as θ_0 is increased. In traces 3–6 of Fig. 13 the ratio $\theta(2)/\theta(1) = 0.46,\ 1.17,\ 1.64,\ 2.27$, respectively, indicating that a steady state is not attained. The total area also increases monotonically as seen in Fig. 14 which shows the energy leveling off to $\mathcal{T} = \mathcal{T}_0' \cong \mathcal{T}_0 e^{-\alpha_s L}$, but no stable θ region. (Note that the data points at lowest θ_0 in Fig. 14 correspond to the second trace of Fig. 13, while the highest θ_0 is not shown in Fig. 13.)

These data exhibit transparency at high powers; the output energy is the same as the input, while the delay, indicative of a coherent interaction, persists. Extreme narrowing is also present and causes the peak of the highest power "on-resonance" pulse of Fig. 13 to be larger than the "off-resonance" peak while their integrated energies are the same.

In addition to the distortion and modulation, we have observed considerable variation in the behavior of $\mathcal{T}$ and θ, as well as in the onset of pulse break up, among different experimental runs and also, as a function of H in any particular run.[26] It was possible to find magnetic field values, on the side of the resonance line, at which the pulse broke up into as many as four separate pulses, as well as other values at which no break up was observed.

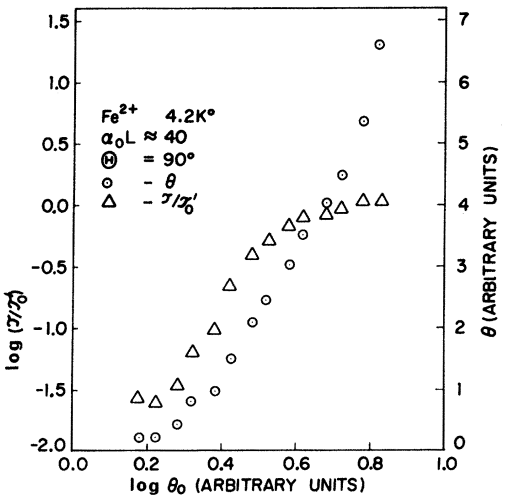

FIG. 14. Measured relative pulse energies and areas from the data of Fig. 13 on Fe^{2+} in sample 3 with parameters shown, $\mathcal{T}_0' = \mathcal{T}_0 e^{-\alpha_s L}$.

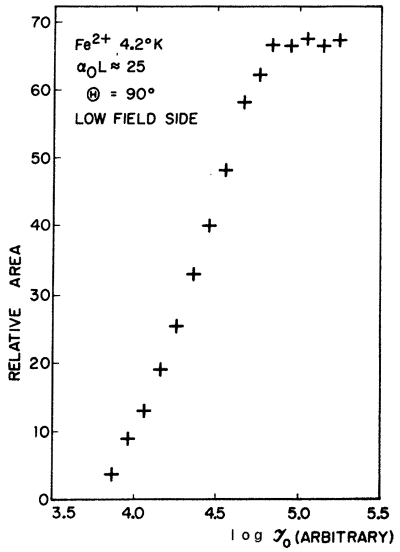

FIG. 15. Measured relative pulse areas versus relative input energies on low-field side of Fe^{2+} resonance in sample 3 with parameters shown.

Figure 15 is a plot of θ versus $\log_{10} \mathcal{T}_0$, taken at one of the latter positions on the low-field side. With increasing $\mathcal{T}_0$ there is a sudden transition to a stationary value of θ, indicating development of a true steady-state pulse. However, $\mathcal{T}$ (not shown) continues to increase through the stable θ region, rather than reaching an extremum as would be expected in the steady state. The relative behavior of θ and $\mathcal{T}$ is thus almost the reverse of that shown in Fig. 14, illustrating the extreme variability mentioned above.

V. DISCUSSION

A. Multiple Passes

An important result of this paper is the steady state approached by the pulse velocity, attenuation, and shape, in the case of multiply reflected echoes. We may term this a quasi-steady-state to differentiate it from the solutions of Eq. (24). In the quasi-steady-state the area is clearly not constant, nor are $\mathcal{T}$ and θ stationary with respect to θ_0. However, the 5.5- and 7.5-dB data of Fig. 11(b) have almost equal slopes, indicating that the pulse velocity goes through a stationary value in the associated range of θ_0.

The theoretical results of Sec. II (Fig. 3) show that the additional delay in the reflected pass is approximately equal to the delay in the first traversal, at high-input intensities for which $\theta_0 > \theta_2$.

Further computation is necessary to see whether this behavior continues for additional reflections. However, in view of the discussion below, formation of even a quasi-steady-state is surprising.

B. Comparison with Theory

While there is good qualitative agreement between the theory of Sec. II and the Ni^{2+} experiments, there are several quantitative discrepancies: No region of stationary θ and concomitant minimum energy loss was observed. At the value $\theta_0 = \theta_2$, for which these are theoretically expected, the measured θ were smaller than theory by a factor 2; the observed maximum DT and τ_H were also smaller than predicted by a factor 2.

Any error in the measured value of α_s, which was used by Hopf in the calculation, cannot be the source of the disagreement. As stated earlier, this value is an upper limit; if the experimental value were actually smaller, coherence phenomena would have been accentuated in the experiment, relative to theory. From the discussion in Sec. IV on the effects of T_2 and τ_0, the deviation of the latter from that used in the computation also would not appear to explain the disparity between theory and experiment.

Standing waves. Although increasing τ_0 in the 1.8 °K experiments had almost no effect, the neglect of standing waves in the theory might still produce an appreciable discrepancy with experiment. Changing the size of the standing-wave regions will affect the results only if the remainder of the propagation path is sufficiently reduced so that the pulse can no longer closely approach its steady-state condition; i.e., if the reduced path is largely a transient regime insofar as reshaping is concerned. According to computer solutions given in MH and by Rhodes and Szöke,[21] only a very few absorption lengths are required for the pulse to reshape. In the present case, a reduction of 25% (due to increasing τ_0 by 0.45 μsec) still leaves a reduced traveling wave-propagation path of about seven absorption lengths, and therefore any standing-wave effects would be nearly independent of pulse length while possibly affecting the experimental observations appreciably.

Non-plane-wave propagation. In their experiments MH also found that experimental θ's were smaller than expected from theory, and have discussed a number of additional causes for disparity with the theory of ideal SIT. These are primarily due to deviations from plane-wave propagation in the experiments. The effect of multipath transmission in distorting the pulse has already been mentioned in Sec. IV. Non-plane-wave character also exists in the acoustic experiments because of guided wave propagation. The well-known beating effect in multiple-echo experiments is partially due to interference of wave-guide modes.[27]

For the problem of uniform excitation (in both amplitude and phase) of longitudinal polarization at one end of a rectangular parallelopiped, the mode solutions are

$$e(x, y, z, t) = e_{n,m}(z, t)\cos(n\pi x/2a)\cos(m\pi y/2b),$$

$$n, m = 1, 3, 5 \ldots 2a \text{ and } 2b$$

are the x and y dimensions, respectively, and $e_{n,m}(z, t)$ has the form of Eq. (6) with $\phi(z)$ different for each mode. If we consider only the lowest mode, $n = m = 1$, and carry out the integrations indicated in MH for the case of a single mode, then in place of the area theorem of Eq. (24) we find

$$\frac{dA}{dz} = -\tfrac{1}{2}\alpha_0 J_0(\tfrac{1}{2}A)J_1(\tfrac{1}{2}A) - \tfrac{1}{2}\alpha_s A\,. \tag{26}$$

$A = \theta(z)$ is the pulse area on the axis $x = y = 0$. At any other point

$$\frac{d}{dz}\,\theta(x, y, z) = \frac{dA}{dz}\,\cos\frac{\pi x}{2a}\cos\frac{\pi y}{2b}\,. \tag{27}$$

There are no steady-state solutions to Eqs. (26) and (27) unless $(\alpha_0/\alpha_s) > 67$, which requires $\alpha_0 L > 108$ if $\alpha_s L = 1.6$. Even if there were a factor 8 reduction in α_s, the lowest steady-state solution would be barely observable in the case of Ni^{2+} and not at all for Fe^{2+} as explained at the end of Sec. III. Since the higher-order solutions require even larger α_0/α_s, they would also not be observable.

While it is not correct to consider only the one mode, even though it carries 80% of the energy, it is clear that guided wave propagation in the experiments can cause large deviations from plane-wave theory. It may also be a cause of the variable effects of crystal alignment and refraction in Fe^{2+} experiments, mentioned earlier, since nonuniform excitation will introduce different sets of modes under differing experimental conditions.

C. Comparison with Previous Results

The delay time expected from the linear theory[2] is $DT \approx \alpha_0 L/2\delta$. As shown in Ref. 1, δ may be the observed inhomogeneous linewidth, or only the contribution from the static part of the dipolar interaction, depending on the spatial scale of the inhomogeneities. In the author's earlier work[1] approximate agreement with the above formula was obtained if it was assumed that only the dipolar contribution was important. In the present experiments on Ni^{2+}, with α_0 an order of magnitude greater than formerly, no delay was observed in the linear region. Therefore, the earlier measurements must be considered as having been made in the transient

regime ($\alpha_0 \approx 1$) of SIT, and their agreement with the linear theory fortuitous. However, at least qualitatively, the present results also have shown that DT is a direct function of T_2 (at least for short T_2)[28] and a comparison of Figs. 7 and 8 shows that for a T_2 ratio of 1.6, the ratio of the DT's is 1.2.

The previous measurements on Fe^{2+} were all made at small angles Θ in the regime of "effective" saturation mentioned in Sec. III. The small delays observed ($DT < \tau_0$) were presumably the apparent delay of the pulse peak in saturation. Since the latter is proportional to $\alpha_0(\Delta H)$, the line shape was reproduced in the delay data, as expected also in the linear theory.

Symmetric pulse shapes were not observed in the previous experiments due to the use of narrow-band cavities and i.f. detectors. It is probably also for this reason that the pulse distortion observed by others[23-25] in Fe^{2+} experiments did not show clear separation of the pulses under break up, as is seen in Fig. 13.

The apparent amplification at high-input powers on Fe^{2+}, reported by Rampton and Rowell,[24] was most probably due to extreme pulse narrowing ($\tau_H < \tau_0$) in the transparency region, as in Fig. 13.

Pulse narrowing, when θ_0 lies between a given θ_2 and the next larger θ_1, is in accord with theory and is exhibited by the computer solutions in MH; however, this "coherence narrowing" has not been observed previously. Patel and Slusher[29] reported pulses having $\tau_H < \tau_0$ in optical experiments on SF_6, but this appears to be the narrowing associated with saturation. [*Note added in proof.* Narrowing was recently reported in an optical experiment; H. M. Gibbs and R. E. Slusher, Phys. Rev. Letters 24, 638 (1970).]

Rhodes and Szöke,[21] also working with SF_6, have measured delay times as a function of input intensity and these results are very similar to the present ones on Ni^{2+}. However, because of the influence of level degeneracy many of the other features of SIT, such as symmetric pulses and transparency, were not observed. Apparent pulse break up in their experiments was found to be due to filamentary transmission.

VI. CONCLUSIONS

The principal features of the theory of SIT, as derived by MH,[4] are exhibited by acoustic pulses propagating in a resonantly absorbing medium. Pulse delay and reshaping have both been observed and are, within a factor 2, in agreement with a calculation by Hopf which approximates the particular experimental arrangement utilized in these experiments. Near transparency was observed at high-input intensities.

A new and important result of this work is the observation that the pulse delay, in SIT, is cumulative over successively reflected traversals through the resonant medium.

Coherence-induced pulse-break-up phenomena were observed and shown to be, at least partially, the cause of modulation, distortion, and apparent amplification which occur in APR experiments on Fe^{2+}.

As explained in Sec. IV, Fe^{2+} is an almost ideal system for studying SIT. Many of the difficulties associated with the present measurements would be obviated by the use of optical Bragg scattering techniques to observe the acoustic pulses. In such experiments it should be possible to study the z and t dependence of the coherent interaction, rather than being limited to observing only the output pulse as in the optical and present acoustic work. The technique also allows measurements of acoustic beam profiles so that the effects of non-plane-wave character could be assessed.

ACKNOWLEDGMENTS

It is a pleasure to acknowledge the invaluable assistance of T. G. Kazyaka in the experiments and with much of the data reduction. The author wishes to express his gratitude to Dr. F. Hopf, of AFRCL, for his calculations of SIT in single and double traversals. The author has also had the benefit of several valuable discussions with Dr. J. A. Armstrong, concerning coherent interactions, in general, and the physical nature of the solutions to Eq. (24), in particular.

APPENDIX

In the limits $T_1 \ll \tau_H(z)$ and $T_1^{-1} \gg (1/\mathcal{E})\partial\mathcal{E}/\partial t$, the steady-state solutions of the Bloch equations [Eqs. (14)] obtain

$$V = -2\kappa \mathcal{E} W_0 T_2/(1 + \Delta\omega^2 T_2^2 + 4\kappa^2 \mathcal{E}^2 T_1 T_2) \quad , \tag{A1}$$

$$U = 2\kappa \mathcal{E} W_0 T_2^2 \Delta\omega/(1 + \Delta\omega^2 T_2^2 + 4\kappa^2 \mathcal{E}^2 T_1 T_2) \, . \tag{A2}$$

These results may be inserted into Eqs. (17) and (18), and the latter solved for the absorption and dispersion. Alternatively, Eq. (10) may be used directly to obtain a dispersion relation for APR. We assume that the predominant spatial and temporal variations in e are just those due to absorption; i.e.,

$$\alpha \mathcal{E}(0, t) \gg \frac{1}{c} \frac{\partial \mathcal{E}(0, t)}{\partial t} \, .$$

Then Eq. 10, for e_+, is

$$-k^2 e_+ + (\omega^2/c^2) e_+ = +(k^2/\rho c^2) R_+ . \tag{A3}$$

Using Eqs. (A1) and (A2) in Eq. (15), for R_+, cancelling e_+ from both sides of Eq. (A3), and rearranging, we have

$$k^2=\frac{\omega^2}{c^2}\left(1+\frac{\hbar\kappa^2 W_0 T_2}{\rho c^2(1+\Delta\omega^2 T_2^2+4\kappa^2\mathcal{E}^2 T_1 T_2)}\ (\Delta\omega T_2-i)\right)^{-1}. \tag{A4}$$

The dispersion relation found earlier by Jacobsen and Stevens,[8] using a different formalism, reduces to Eq. (A4) when $\Delta\omega \ll \omega$ and saturation terms, included here, are neglected. In the small-signal limit, and for $|k-\omega/c| \ll k$, the amplitude attenuation is given by

$$\mathrm{Im}\, k=\hbar\kappa^2 W_0 T_2\omega/2\rho c^3(1+\Delta\omega^2 T_2^2).$$

When this is averaged over the distribution of resonant frequencies[30] the absorption constant $\alpha_0(\Delta\omega)$ is obtained,

$$\tfrac{1}{2}\alpha_0(\Delta\omega)=-\pi\hbar W_0\kappa^2\omega g(\Delta\omega)/2\rho c^3. \tag{A5}$$

---

*Parts of this paper were written while the author was on leave as a guest at The Clarendon Laboratory, University of Oxford, Oxford, England, with partial support from a John Simon Guggenheim Memorial Fellowship.

[1]N. S. Shiren, Phys. Rev. 128, 2103 (1962).

[2]L. Brillouin, *Wave Propagatjon and Group Velocity* (Academic, New York, 1960); and H. Baerwald, Ann. Physik 7, 731 (1930).

[3]P. F. McDonald, U. S. Army Missile Command Report No. RR-Tm-68-1, 1968 (unpublished).

[4]S. L. McCall and E. L. Hahn, Phys. Rev. 183, 457 (1969).

[5]F. A. Hopf and M. O. Scully, Phys. Rev. B 1, 50 (1970).

[6]F. A. Hopf, Phys. Rev. (to be published). I am indebted to Dr. Hopf for allowing me to use his results prior to publication.

[7]C. K. Rhodes, A. Szöke, and A. Javan, Phys. Rev. Letters 21, 1151 (1968).

[8]E. H. Jacobsen and K. W. H. Stevens, Phys. Rev. 129, 2036 (1963).

[9]D. H. McMahon, Phys. Rev. 134, A128 (1964).

[10]See C. Kittel, Rev. Mod. Phys. 21, 541 (1949); and T. G. Phillips and R. L. White, Phys. Rev. 153, 616 (1967).

[11]For the $\Delta\langle S_z\rangle=2$ transition, U and V are not components of the magnetization in the rotating frame, but are, respectively, $\langle S_x'^2-S_y'^2\rangle$ and $\langle S_x' S_y'+S_y' S_x'\rangle$. W is still $\langle S_z'\rangle$ and $U^2+V^2+W^2=S(S+1)$.

[12]S. R. P. Smith, F. Dravnieks, and J. E. Wertz, Phys. Rev. 178, 471 (1969). Our T_1 and T_2 are given, in the notation of this reference, by $(2/T_3-1/T_1)^{-1}$ and $(1/T_s+1/T_3)^{-1}$, respectively.

[13]E. H. Jacobsen, J. Acoust. Soc. Am. 32, 949 (1960).

[14]Restricting the calculation to the single longitudinal strain, e_{zz} is equivalent to assuming that it is a normal propagating mode in the paramagnetic sample. This assumption is not valid; it may be shown, quite generally, that the normal modes have elliptical polarizations, in the presence of magnetic fields. [K. B. Vlasov, Izv. Akad. Nauk SSSR, Ser. Fiz. 22, 1159 (1958).] The components $R_{ij}=N\,\mathrm{Tr}[+(\partial H_c/\partial e_{ij})\sigma]$, $(ij\neq zz)$, which can be calculated by utilizing the full Hamiltonian, Eq. (3), rather than the truncated form, Eq. (5), are nonzero and provide source terms for wave equations in the transverse polarizations. These latter should, therefore, be included at the start. However, direct calculation also shows that, at least for normal incidence on an acoustic axis, the resulting e_{ij} are always smaller than e_{zz} by a factor of order α/k, and therefore negligible within the spirit of the slowly varying envelope approximation.

[15]F. A. Hopf and M. O. Scully, Phys. Rev. 179, 399 (1969).

[16]L. M. Frantz and J. S. Nodvick, J. Appl. Phys. 34, 2346 (1963).

[17]R. Bellman, G. Birnbaum, and W. G. Wagner, J. Appl. Phys. 34, 779 (1963).

[18]The arguments given by A. Szöke and E. Courtens, Phys. Letters 28A, 296 (1968) do not apply when $T_2^*\ll T_2$, except on the edges of the line where homogeneous broadening may dominate.

[19]N. S. Shiren, Bull. Am. Phys. Soc. 14, 392 (1969); and (unpublished).

[20]R. Loudon, Phys. Rev. 119, 919 (1960), and Ref. 1, Appendix.

[21]C. K. Rhodes and A. Szöke, Phys. Rev. 184, 25 (1969).

[22]N. S. Shiren, Phys. Rev. Letters 11, 3 (1963).

[23]J. K. Wigmore and H. M. Rosenberg, Phil. Mag. 15, 701 (1967).

[24]V. W. Rampton and P. M. Rowell, Phys. Letters 7, 12 (1963).

[25]R. Guermeur, J. Joffrin, A. Levelut, and J. Penne, Phys. Letters 15, 203 (1965).

[26]See also Ref. 24.

[27]E. H. Jacobsen, in *Proceedings of the First International Conference on Quantum Electronics* (Columbia U. P., New York, 1960).

[28]The values of T_2 calculated in Ref. 1 include both the static and dynamic parts of the spin-spin interaction, whereas in the measurements reported here, only the dynamic part (which contributes to loss of phase memory) is included and is considerably reduced by the strain-induced inhomogeneous broadening. See W. B. Mims, *Electron Paramagnetic Resonance* (Plenum, New York, 1970).

[29]C. K. N. Patel and R. E. Slusher, Phys. Rev. Letters 19, 1019 (1967).

[30]A. M. Portis, Phys. Rev. 91, 1071 (1953).

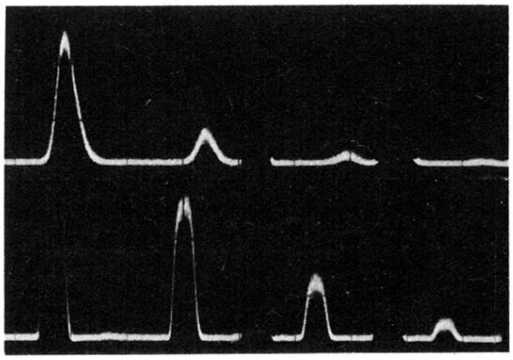

FIG. 11. Oscilloscope traces showing four complete round trips in the MgO. Time increases from left to right, 1 sec per division. Upper trace: ultrasonic frequency on Ni^{2+} resonance. Lower trace: off-resonance. Two echoes resulting from a round trip in the quartz transducer have been blocked out.

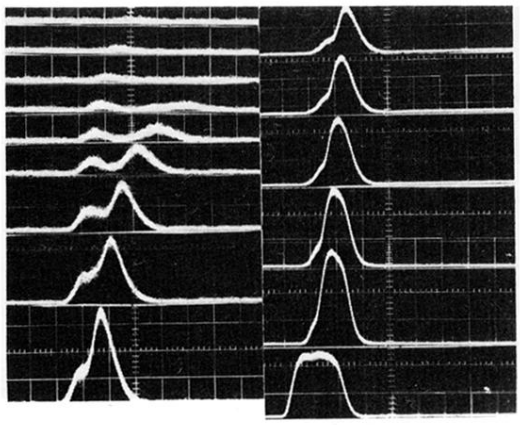

FIG. 13. Oscilloscope traces showing pulse break up due to interaction with Fe^{2+} resonance in MgO sample 3 with parameters given in Fig. 14. Input power increases from top to bottom in each column. Detector gain 8 dB higher on left than on right. Last trace shows off-resonance pulse at same input-power and gain settings as immediately preceding trace.

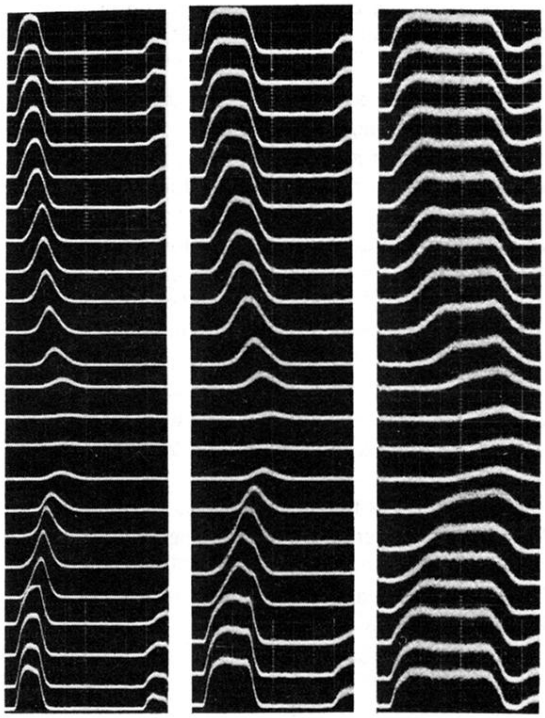

FIG. 4. Oscilloscope traces showing changes in pulse shape and delay as magnetic field is scanned (increasing from top to bottom) across Ni^{2+} transition in MgO sample 2 at 1.8 °K. Three input pulse widths are shown from left to right; $\tau_H(0) = 0.45$, 0.9, and 2.1 μsec. Time increases from left to right in each trace. A second round-trip echo may be seen on some traces. Off-resonance pulses shown at bottom of each set.

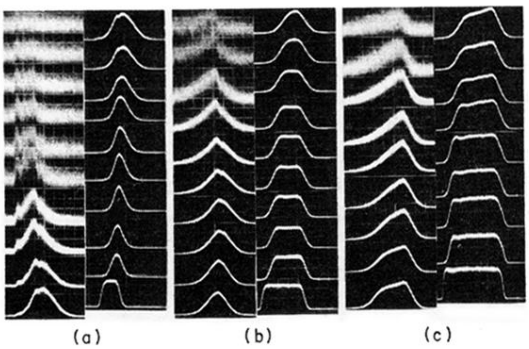

FIG. 5. Oscilloscope traces showing changes in pulse shape and delay as input power is increased (top to bottom in each column). Ni^{2+} resonance in MgO sample 1 at 4.2°K, $\tau_H(0)$ = (a): 0.4 μsec, (b): 0.87 μsec, (c): 2.3 μsec. Where possible, detector gain was adjusted to keep output amplitudes constant. Off-resonance pulses shown at bottom right of each set.